CELL BIOLOGY

Mechanistic insights into the SNARE complex disassembly

Xuan Huang¹*[†], Shan Sun¹*, Xiaojing Wang¹*, Fenghui Fan¹*, Qiang Zhou¹*, Shan Lu², Yong Cao², Qiu-Wen Wang³, Meng-Qiu Dong², Jun Yao³, Sen-Fang Sui¹§

NSF (N-ethylmaleimide–sensitive factor) and α -SNAP (α -soluble NSF attachment protein) bind to the SNARE (soluble NSF attachment protein receptor) complex, the minimum machinery to mediate membrane fusion, to form a 20S complex, which disassembles the SNARE complex for reuse. We report the cryo-EM structures of the α -SNAP–SNARE subcomplex and the NSF-D1D2 domain in the 20S complex at 3.9- and 3.7-Å resolutions, respectively. Combined with the biochemical and electrophysiological analyses, we find that α -SNAPs use R116 through electrostatic interactions and L197 through hydrophobic interactions to apply force mainly on two positions of the VAMP protein to execute disassembly process. Furthermore, we define the interaction between the amino terminus of the SNARE helical bundle and the pore loop of the NSF-D1 domain and demonstrate its essential role as a potential anchor for SNARE complex disassembly. Our studies provide a rotation model of α -SNAP–mediated disassembly of the SNARE complex.

Copyright © 2019
The Authors, some rights reserved; exclusive licensee
American Association for the Advancement of Science. No claim to original U.S. Government Works. Distributed under a Creative
Commons Attribution
NonCommercial
License 4.0 (CC BY-NC).

INTRODUCTION

Membrane fusion is one of the critical steps of vesicular trafficking. It is highly conserved during the evolution of the eukaryotic cells (1). The SNARE (soluble *N*-ethylmaleimide–sensitive factor attachment protein receptor) complex, composed of v-SNARE on the membrane of a vesicle and t-SNARE on the target membrane, is a highly stable four-helix bundle (2) that drives the membrane fusion (2-4). The SNARE complex that mediates synaptic exocytosis consists of one v-SNARE [vesicle-associated membrane protein (VAMP), also known as synaptobrevin] and two t-SNAREs [syntaxin and synaptosomeassociated protein 25 (SNAP25)] (5). α -SNAP (α -soluble Nethylmaleimide-sensitive factor attachment protein) and NSF (N-ethylmaleimide–sensitive factor), the latter being a type II AAA+ [adenosine triphosphatase (ATPase) associated with various cellular activities] ATPase, sequentially bind to the SNARE complex to form a 20S complex in which NSF, upon using the energy from adenosine 5'-triphosphate (ATP) hydrolysis, disassembles the SNARE complex to recycle the subunits (6-11).

Over the past few decades, biochemical and structural studies have provided valuable insights into the structures and functions of the individual components of the 20S complex. The crystal structures of several SNARE complexes (2, 12–17) indicate that the core region of the SNARE complex consists of 16 layers including a highly conserved central ionic zero layer embedded within 15 hydrophobic layers, thus maintaining its high stability (2). Studies of the NSF protein (18, 19) identified functional roles for many of the structural

elements of the N domain (20-24) and the D1D2 ring (23-26). For instance, mutations of the conserved YVG motif, which is present only in the central pore of the catalytically active D1 domain, rendered NSF defective in the SNARE complex disassembly (23). However, because of the lack of structural information, how this structural element assists the dissociation of the SNARE complex remains unclear. For SNAP, structural studies have revealed a twisted sheet of α -helical hairpins and an α -helical bundle in its N- and C-terminal regions, respectively (27, 28). Except for the extensive studies of the individual components of the 20S complex, the cryo-electron microscopy (cryo-EM) structures of the whole 20S complex at medium resolutions were reported by our group and the other group independently in 2015 (29, 30). Both works showed four α-SNAPs wrapping around the single left-handed SNARE helical bundle as a right-handed cylindrical assembly within a 20S particle (29, 30). However, because of the limited resolution (29–33), pivotal questions remain unaddressed, such as the following: What are the interactions between α-SNAPs and individual SNARE proteins that directly cause SNARE complex disassembly? Onto which part(s) of the SNARE complex do SNAPs exert disassembly force?

RESULTS

Cryo-EM structure of the nanodisc-20S particle

To answer these questions and to elucidate the molecular mechanism of the SNARE complex disassembly, it is critical to improve the structure of the 20S complex at high resolution. Previously, we used carbon film—coated grids to enrich the nanodisc-20S particles for the cryo-EM reconstruction (30). To improve the cryo-EM image quality, we increased the concentration of the complex for cryo-EM specimen preparation so that a sufficient number of nanodisc-20S particles entered ice without carbon film support. This condition increased the contrast of the image and eliminated the orientation preference that we previously encountered. As a result, we were able to reconstruct the ADP-AlFx bound nanodisc-20S particle with an overall resolution of 4.6 Å from ~7000 micrographs (fig. S1). We used the same particle segmentation method that we have previously developed (30, 34) to improve the resolution of the α -SNAP–SNARE and NSF-D1D2

¹ State Key Laboratory of Membrane Biology, Beijing Advanced Innovation Center for Structural Biology, School of Life Sciences, Tsinghua University, Beijing 100084, China. ²National Institute of Biological Sciences, Beijing 102206, China. ³ State Key Laboratory of Membrane Biology, Tsinghua-Peking Joint Center for Life Sciences, IDG/McGovern Institute for Brain Research, School of Life Sciences, Tsinghua University, Beijing 100084, China.

^{*}These authors contributed equally to this work.

[†]Present address: Medical Research Center, Beijing Chaoyang Hospital, Capital Medical University, Beijing 100020, China.

[‡]Present address: State Key Laboratory of Membrane Biology, Beijing Advanced Innovation Center for Structural Biology, School of Medicine, Tsinghua University, Beijing 100084, China.

[§]Corresponding author. Email: suisf@mail.tsinghua.edu.cn

subcomplexes separately. This led to the reconstruction of the $\alpha\textsc{-SNAP-SNARE}$ subcomplex at 3.9-Å resolution and the NSF-D1D2 at 3.7-Å resolution without imposing any symmetry after masking out the relatively flexible NSF N domains (figs. S1 and S2). Note that although we used the full-length soluble portion of syntaxin-1A, the Habc domain exhibited no EM density, likely reflecting its dynamic location due to the long linker of $\sim\!40$ residues between the Habc domain and the followed SNARE motif (35). Thus, the signals of the Habc domain were averaged out during the three-dimensional (3D) reconstruction.

Structure of the α -SNAP-SNARE subcomplex

Although the overall structure of the α -SNAP–SNARE subcomplex is similar to what has been previously reported with the characteristic feature of four α-SNAPs wrapping around the single left-handed SNARE helical bundle, the map quality is improved substantially compared to the previous ones. The resolution of certain regions, especially the SNARE complex located at the center, even reached 3.0 Å (Fig. 1A), allowing unambiguous identification of the sidechain densities of most residues within the SNARE core complex. For instance, the R56 at layer zero of the VAMP chain can be discriminated (Fig. 1B). Moreover, we noticed that there is an extended density at the C-terminal portion of one of four SNARE chains (Fig. 1B). This observation is consistent with the composition of the SNARE complex used in the reconstitution system, in which only the VAMP protein still contains the C-terminal transmembrane region and is thus longer than the other three chains. Therefore, the four SNARE chains can be unambiguously distinguished on the basis of the side-chain densities and the longer C terminus of VAMP. It may be noticed that four α -SNAP molecules are bound to the SNARE complex in our structure, which is in contrast to two α -SNAP molecules bound to the SNARE complex described in the recent work reported by White et al. (36) during the revision of our manuscript. The difference may be due to the fact that our structure was resolved with the membrane-anchored 20S complex—a near-native state of the 20S complex, and the presence of a membrane is known to increase the affinity of α -SNAP for the SNARE complex (37).

Specific interactions between the SNARE complex and α -SNAP

We further analyzed the interactions between α -SNAP and the SNARE complex based on our structure. As shown in Fig. 1C, each α-SNAP molecule interacts with three of four chains of the SNARE complex. In each of the four α -SNAP molecules, almost an identical set of residues makes contact with the SNARE complex, but on the receiving side, different sets of residues are used by individual SNARE chains. Further analysis identified 12 SNARE-interacting residues in α-SNAP, including previously found hydrophobic residues L197, L198, and Y200 (30) and positively charged residues K122 and K163 (Fig. 1C) (29). To corroborate the structural observations, we mutated these residues to alanine and examined their effects on two distinct activities, which are the α-SNAP-dependent binding of NSF to the SNARE complex and the SNARE complex disassembly (Fig. 2A and fig. S3). All mutants showed reduced activity in at least one of the assays, and most of them exhibited impaired activities for both assays. Among all the mutants, two mutations, R116A and L197A, were of special interest because they both had an average effect on the binding activity (31 and 49% of that of wildtype α-SNAP for R116A and L197A, respectively) compared with

their notably low efficiencies on the SNARE complex disassembly (2 and 5% of that of WT α -SNAP for R116A and L197A, respectively), suggesting that these two residues have direct roles in the SNARE complex disassembly.

To further evaluate the functional relevance of R116 and L197 in vivo, we investigated the effects of these mutants on the spontaneous neurotransmitter release of cultured hippocampal neurons. We overexpressed the wild-type α -SNAP and the mutants in hippocampal neurons through lentiviral infection, which was confirmed by the results of immunoblot and quantitative reverse transcription polymerase chain reaction (qRT-PCR) analyses (fig. S4). We then performed whole-cell patch-clamp recording experiments to analyze the frequency and amplitude of miniature excitatory postsynaptic currents (mEPSCs), which have been widely used to evaluate the presynaptic vesicle release velocity and postsynaptic glutamate receptor density, respectively. The results indicated that, compared to the control group without any overexpression, the neurons with wildtype α-SNAP overexpressed showed a greatly increased mEPSC frequency (Fig. 2B). Hence, the wild-type protein could enhance synaptic vesicle exocytosis, probably because the SNARE complex disassembly was accelerated and thus the SNARE proteins could be rapidly reused. However, compared to the wild-type α -SNAP overexpression, the introduction of R116A and L197A showed lower mEPSC frequencies. These results indicated that these two mutants probably weaken the membrane fusion significantly by reducing the capability of the SNARE complex disassembly (Fig. 2B). In all groups, the mEPSC amplitude did not show any obvious difference, indicating that the postsynaptic glutamate receptors were unaffected by the overexpression (Fig. 2B). Thus, both in vitro biochemical experiments and in vivo electrophysiological experiments demonstrated that R116 and L197 play essential roles in the SNARE complex disassembly. Consistent with this, these two residues are highly conserved in α-SNAP among several vertebrate species, and even invertebrates such as Drosophila (fig. S5), further indicating their important roles in the SNARE complex disassembly.

To elucidate how the residues R116 and L197 of α-SNAPs carry out the disassembly of the SNARE complex, we introduced mutations at the residues corresponding to the interacting partner residues of the four SNARE chains (Fig. 2, C and D) and examined the disassembly for each mutant (Fig. 2E and fig. S3). Although all single point mutations nearly showed no influence on the disassembly of the SNARE complex, the multiple point mutations in which all residues of individual SNARE chains involved in the direct interactions with R116 or L197 of α-SNAP were mutated simultaneously did exhibit different effects. In our model, two R116 residues from α -SNAP-H and α -SNAP-E interact with two sites of VAMP, E62 and D68, respectively (Fig. 2C). When both VAMP E62 and D68 were mutated together, the disassembly activity was substantially reduced to only 12% to that of the wild type (Fig. 2E and fig. S3). When VAMP V48, V50, and L54 that interact with two L197 residues from α-SNAP-G and α-SNAP-H were mutated simultaneously, the disassembly activity was reduced to 39% (Fig. 2, D and E, and fig. S3). In contrast, the two residues of SNAP25-N, L47 and M49, which interact with two α -SNAP molecules at site L197, only showed slightly impaired decrease of the disassembly activity (70% to that of wild type) when both mutated. Double point mutation of syntaxin E238 and D242 residues that interact with one α-SNAP molecule at site R116 showed almost no defect in the SNARE complex disassembly. As a control, the binding activities were not reduced in

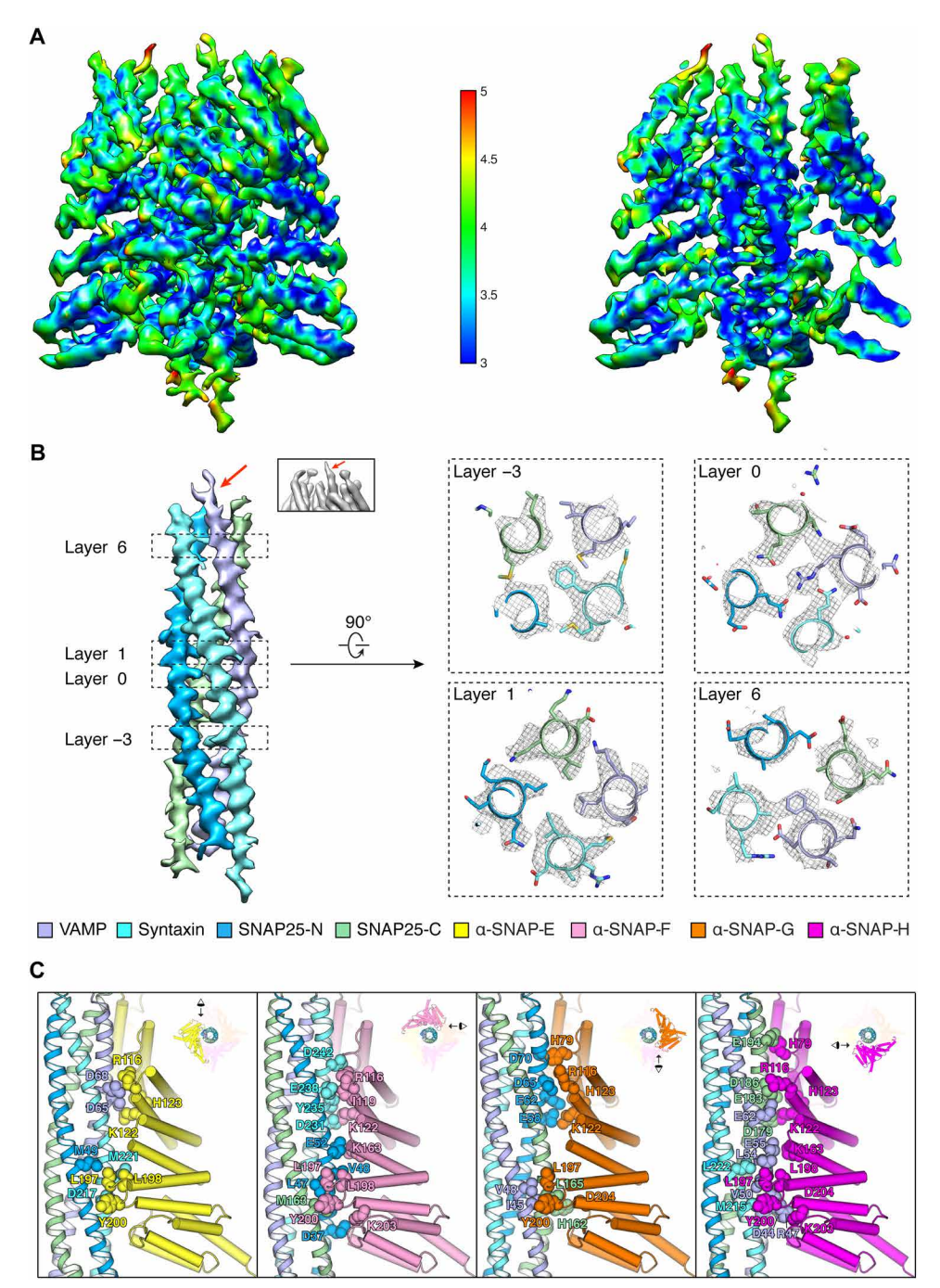


Fig. 1. Structure of the α **-SNAP-SNARE subcomplex.** (**A**) The EM density map of the α -SNAP-SNARE subcomplex color-coded to show the local resolution as estimated by ResMap. The right panel shows a cut-through view of the interior of the map. (**B**) Cryo-EM density (mesh) of representative layers of the SNARE complex superimposed with respective atomic models (stick). Unsharpened map showing the extended density corresponding to the longer C terminus of VAMP is displayed in the inset. The red arrows indicate the extended density. (**C**) Interactions of each α -SNAP with the SNARE complex showing interacting residues. Eye symbols and arrowheads in the insets indicate view directions. Note that each α -SNAP molecule interacts with three of the four chains of the SNARE complex, and in each of the four α -SNAP molecules, almost an identical set of residues make contact with SNARE, but on the receiving side, different sets of residues are used by individual SNARE chains.

the mutants in which VAMP E62 and D68, or VAMP V48, V50, and L54 were mutated (fig. S6). These results indicate that the interactions between VAMP and three of four $\alpha\text{-SNAPs}, \alpha\text{-SNAP-E}, \alpha\text{-SNAP-G},$ and $\alpha\text{-SNAP-H},$ at the sites R116 and L197 on $\alpha\text{-SNAPs}$ and their corresponding sites on VAMP play vital roles in the SNARE complex disassembly.

Direct interaction between the N terminus of the SNARE complex and NSF-D1

Next, we examined the interaction between the N terminus of the SNARE complex and the NSF-D1 ring. Since the α -SNAP-SNARE subcomplex and NSF-D1D2 are relatively flexible with each other, we performed focused classification on the α -SNAP-SNARE subcomplex

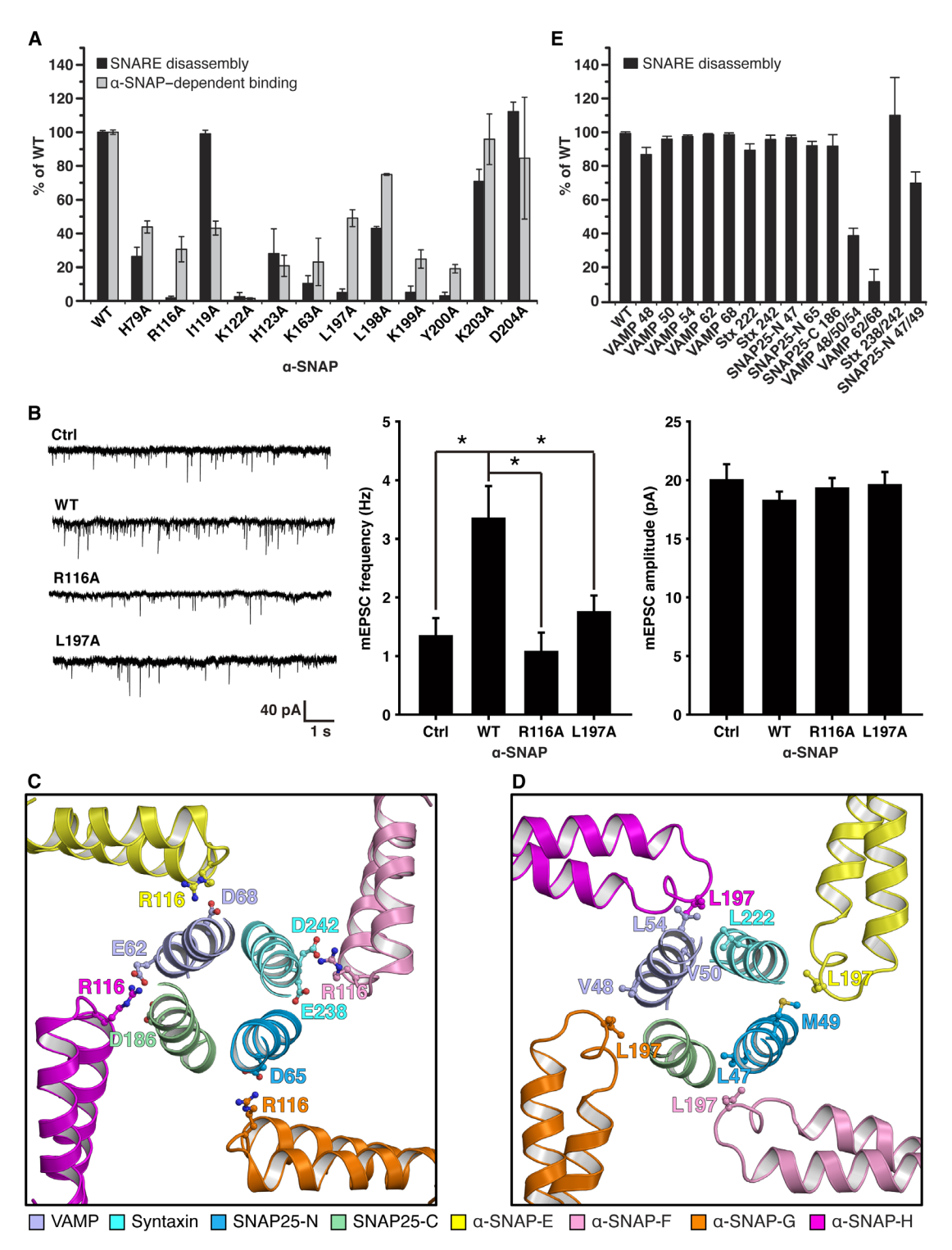


Fig. 2. Essential role of R116 and L197 of α -SNAP in **the SNARE complex disassembly.** (**A**) Effect of α -SNAP mutations on the α -SNAP-dependent binding of NSF to the SNARE complex and the SNARE complex disassembly. Values are normalized to wild-type (WT) α -SNAP and represent the mean \pm SD. (**B**) Significance of α -SNAP R116 and L197 residues for the spontaneous neurotransmitter release. Left panel: representative traces of mEPSCs recorded from cultured WT hippocampal neurons alone (Ctrl), overexpressing WT α -SNAP (WT), and mutated α -SNAPs R116A and L197A. Middle and right panels: quantitative analysis of the frequency (middle) and amplitude (right) of mEPSCs. Shown are the mean \pm SEM. The number of cells/independent cultures analyzed are 18, 22, 16, and 21 for Ctrl, WT, R116A, and L197A, respectively. Statistical assessment was performed by Student's *t* test (**P* < 0.05). (**C**) Interactions between SNAP R116 and the SNARE complex. Note that two R116 residues from α -SNAP-H and α -SNAP-E interact with two sites of VAMP, E62 and D68, respectively. (**D**) Interactions between SNAP L197 and the SNARE complex. Note that two L197 residues from α -SNAP-H interact with three sites of VAMP, V48, V50, and L54, respectively. (**E**) Effect of mutations of individual SNARE proteins on the SNARE complex disassembly. Values are normalized to the WT SNARE complex and represent the mean \pm SD.

together with the NSF N domain based on the angles obtained from the refinement of the segmented D1D2 part (fig. S7A, see Materials and Methods for details). Six distinct groups were identified, and each exhibited a different pattern of the locations of the N domains relative to the asymmetric D1 ring (fig. S7A). Three-dimensional reconstruction of the six classes yielded six asymmetric molecular states of 20S with nearly the same D1D2 conformation but different N domain and SNARE complex positions relative to the D1 ring (fig. S7B). The SNARE complex model was docked into each cryo-EM density map of the six states of 20S and was represented as a cylinder (fig. S7B). When we superposed the six 20S maps, their D1D2 parts were well aligned. However, the positions of the SNARE complexes are obviously different. The SNARE complex's N-terminal region close to the D1 ring is comparatively less displaced among the six states, while the C-terminal region exhibits large diverse positions (Fig. 3, A and B). This phenomenon suggests that a potentially specific interaction between the N-terminal region of the SNARE complex and the D1 ring of NSF may limit the movement of the former to an almost fixed location.

To further investigate the interaction between the SNARE complex's N-terminal region and the D1 ring of NSF, we calculated the distribution of the residue at the SNARE complex's N-terminal region relative to the D1D2 part. According to the unsharpened map of the segmented α -SNAP–SNARE subcomplex, the residues located at the very N terminus of the SNARE complex are from the N-terminal portion of SNAP25-N (Fig. 3C). On the basis of the refinement data of the segmented α -SNAP-SNARE subcomplex, the coordinate of the target residue of the SNARE complex in the micrographs could be identified, from which a map representing the distribution of the target residue relative to the D1D2 part can be reconstructed (see Materials and Methods for details). The result showed that the residue from the very N-terminal region of the SNARE complex is located near the D1 pore loop (YVG motif) of chain E and overlaps with the SNARE complex's N-terminal regions of the six states of the 20S obtained from the focused classification (Fig. 3, A and D to F). Moreover, the shortest distance between the most likely position of the target residue of the SNARE complex (the center of the reconstructed map) and the pore loop is around 5 Å, strongly suggesting a direct interaction between the N-terminal region of the SNARE complex and the pore loop of the NSF-D1 domain (Fig. 3E).

We used mass spectrometry analyses of the 20S complexes crosslinked with either disuccinimidyl suberate (DSS) or 1-ethyl-3-(3-dimethylaminopropyl)carbodiimide (EDC) to further validate our structural analysis (Fig. 3G and tables S2 and S3). DSS is an amine-specific cross-linker with an arm length of 11.4 Å, and EDC is a zero-length cross-linker between amine and carboxyl groups. In the wild-type 20S, both DSS and EDC cross-linked residues localized to the N terminus of the SNARE complex with K293 or E297 of NSF, two residues adjacent to the pore loop. In the mutated 20S particle formed with the N-terminally truncated SNARE complex in which the N-terminal sequence before the two amino acids leading up to the layer -7 of each SNARE proteins was deleted (fig. S8 and table S3), only DSS (and not EDC) was able to cross-link the N terminus of the SNARE complex with the pore loop region of NSF-D1 (Fig. 3G and tables S2 and S3). These results indicate that the distance between the SNARE complex and the pore loop of NSF is larger in the mutated 20S with truncated SNARE proteins than in the wild-type 20S. This suggests that the interaction between the two regions, which we suspect to be necessary for disassembly of the SNARE complex, is weakened in the mutated 20S complex with truncated SNARE proteins. In agreement with this idea, the SNARE complex could not be disassembled when supplied with ATP and Mg²⁺ in the mutated 20S complex with truncated SNARE proteins (Fig. 3H). This supports the idea that the interaction between the N terminus of the helical bundle of SNARE and the D1 pore loop of NSF is essential for SNARE disassembly, possibly by acting as an anchor in the disassembly process.

DISCUSSION

Our current work revealed more details of the interactions between SNAP and the SNARE complex than the previous reports and led to a possible model of the SNARE complex disassembly (Fig. 4). Located at the center, the four α -helix bundle of the SNARE complex has a left-handed orientation in contrast to the right-handed barrel formed by the four α -SNAPs wrapping around it (29, 30). Such an α -SNAP-SNARE assembly with opposite twists suggests that some kind rotation is involved in the process of the SNARE complex disassembly. Such a rotation was observed in the NSF-D1 ring, which rotates counterclockwise relative to the NSF-D2 ring along the central axis upon ATP hydrolysis (33). In one 20S complex, there are six NSF molecules and four α-SNAP molecules. This symmetry mismatch is such that the individual α-SNAP monomers are bound to either one or two nearby NSF N domains and thus would produce various possible modes when the α -SNAP-SNARE subcomplex is engaged by the NSF hexamer. Six distinct states of 20S were identified in our work (Fig. 3 and fig. S7), and each state exhibits a unique interaction pattern between α-SNAPs and NSF N domains, as well as a unique orientation of the α-SNAP-SNARE subcomplex relative to the NSF-D1D2 ring. This correlation between the direction of the α-SNAP-SNARE subcomplex and the interaction mode of the α-SNAP with the NSF N domain strongly argues that the different patterns of α -SNAP/N domain interaction account for the different orientations of the α-SNAP-SNARE subcomplex. Furthermore, because of the interactions with α -SNAP molecules, the NSF N domains are immobilized in the 20S complex, which is evidenced by the notably better-defined densities of the six N domains of NSF in 20S than those of ATP- and ADP-bound NSF alone (our structure and the work from other group) (29). This phenomenon suggests that once binding to the substrate, NSF N domains would become stable enough relative to the D1 ring, therefore allowing the motion transmission from D1 to N domains, and eventually to the α-SNAP barrel since the N domains of NSF directly interact with the C-terminal regions of α -SNAPs (29). Thus, the rotational motion of the NSF-D1 ring may induce the same rotation of the α -SNAP barrel. This rotation of the α -SNAP barrel may generate mechanical force along the tangent direction of the cylindrical barrel, applying mainly on two sites of VAMP based on our current work. The two sites correspond to their respective interacting residues on the α-SNAP, where one site interacts with the R116 residue and the other interacts with L197. Since the N terminus of the SNARE complex is directly anchored to the pore region of the NSF-D1, the right-handed torque generated upon ATP hydrolysis would start to unwind and/or break the left-handed helical SNARE complex and thus disassemble the complex into individual proteins. Certainly, some other forces such as pulling and sliding may also help to disassemble the SNARE complex. Nevertheless, the possibility of other

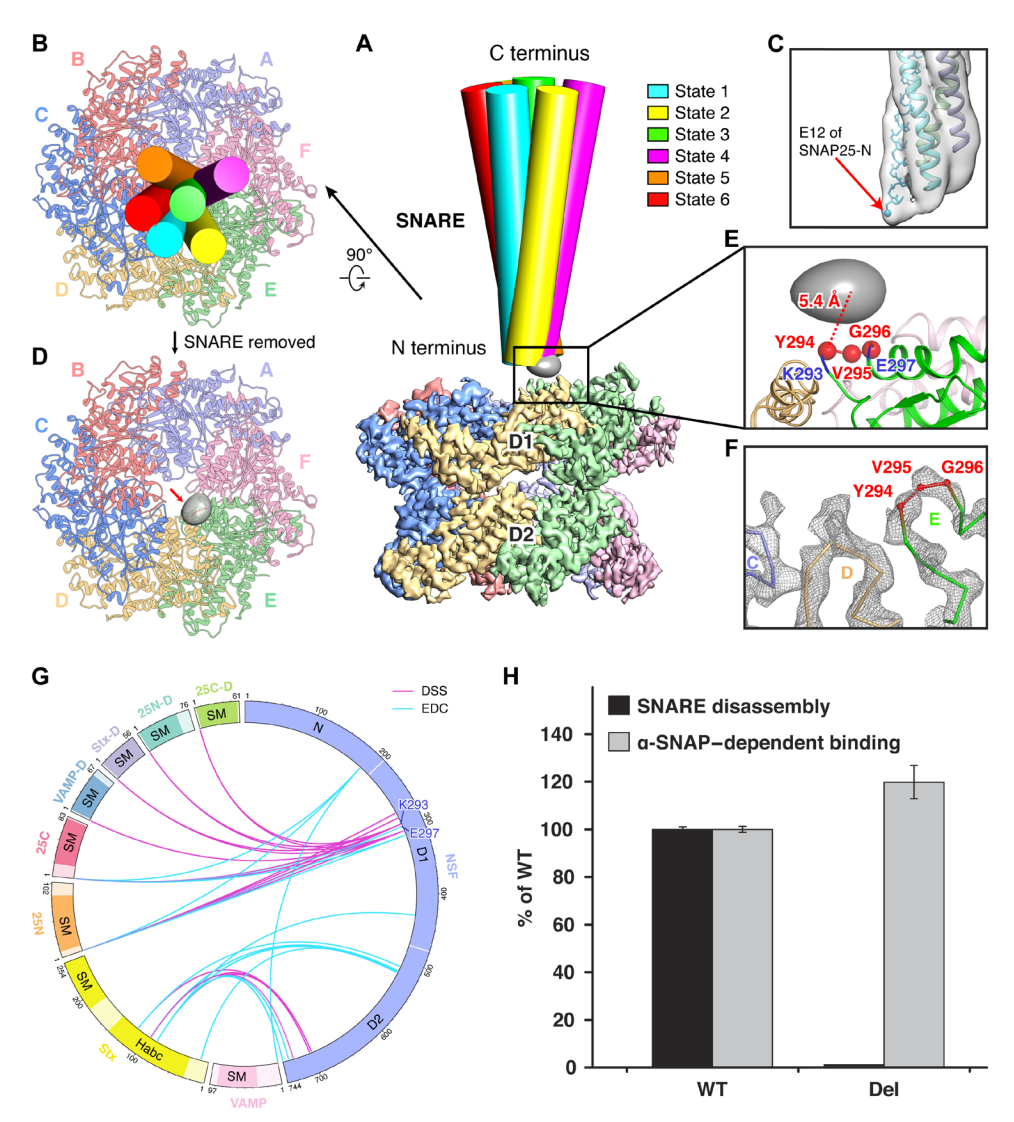


Fig. 3. Direct interaction between the N terminus of the SNARE complex and NSF-D1. (A) Different positions of the SNARE complexes relative to the D1 ring in the six states of the 20S complex. The identified six states were aligned with respect to the D1D2 rings. The SNARE complex is represented as a cylinder. The volume in gray at the bottom of the SNARE complexes represented the distribution of the residue E12 from SNAP25-N. (B) Top view of (A) showing the relative positions between the SNARE complexes and the D1 ring. (C) Unsharpened density map of the SNARE complex superimposed with the model. The red arrow indicates the residue located at the very N terminus of the SNARE complex. (D) Top view of (A) with the SNARE cylinders omitted. Note that the volume (gray) representing the distribution of the residue E12 from SNAP25-N overlaps with the D1 pore loop (red) of chain E (red arrow). (E) Volume representing the distribution of the residue E12 from SNAP25-N is close to the YVG motif (red spheres). NSF K193 and E297 (blue) were found cross-linked to the N terminus of the SNARE complex from 20S treated with chemical cross-linkers. (F) Cryo-EM density (mesh) of the D1 pore loops superimposed with the atomic model (stick) showing the quality of the EM map at the D1 pore loops. (G) Summary of the chemical cross-linking results. Circular plot showing the distribution of the identified cross-linked residue pairs (tables S2 and S3) mapped to protein sequences. VAMP, Stx, 25N, and 25C are the WT VAMP, Syntaxin, SNAP25-N, and SNAP25-C proteins, respectively. VAMP-D, Stx-D, 25N-D, and 25C-D are the N-terminally deleted VAMP, Syntaxin, SNAP25-N, and SNAP25-C proteins, respectively. Note that only DSS (and not EDC) was able to cross-link the N terminus of the SNARE complex with the pore loop region of NSF-D1 in the mutated 20S particle formed with four N-terminally deleted SNARE chains. (H) Effects of the deletion of the N termini of the four SNARE chains (del) on the α-SNAP-dependent binding of NSF to the SNARE complex a

models still need to be considered, such as the alternative rotation model in which the rotation of the SNARE complex induced by the D1D2 rings within a relatively stationary NSF barrel would produce the required torque to unwind the SNARE complex. However, the detailed interactions between the SNARE complex and the pore loops of NSF-D1 from high-resolution structures would be required to test this hypothesis.

Nevertheless, there are still many remaining questions. One important question is whether the four SNARE chains are separated simultaneously or sequentially. As revealed in this work, α -SNAPs applied forces mainly on VAMP. Therefore, one would expect that VAMP might be the first to be disassembled from the SNARE complex. However, it is also possible that the four SNARE chains would dissociate at the same time. Other techniques will be needed to answer this question.

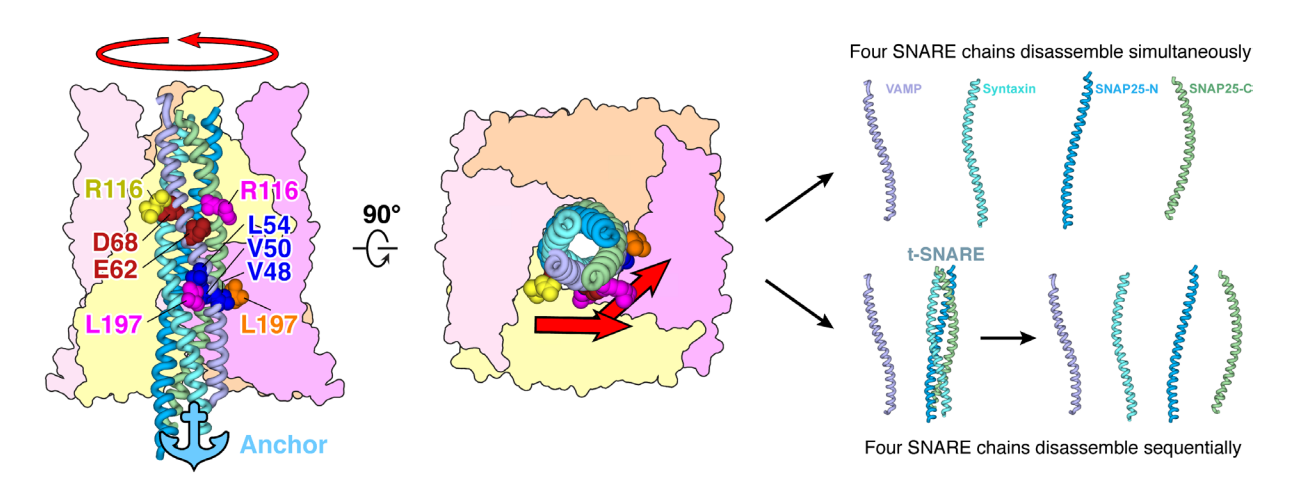


Fig. 4. Model of the SNARE complex disassembly. The rotation of the α -SNAP barrel induced by the rotation of the NSF-D1 ring upon ATP hydrolysis may generate mechanical force along the tangent direction of the cylindrical barrel, applied mainly on two sites of VAMP. These two sites correspond to their respective interacting residues on the α -SNAP, where one site interacts with the R116 residue and the other interacts with L197. Since the N terminus of the SNARE complex is directly anchored to the pore region of the NSF-D1, the right-handed torque would start to unwind and/or break the left-handed helical SNARE complex and thus disassemble the complex into individual proteins simultaneously or sequentially.

MATERIALS AND METHODS

Preparation of the nanodisc-20S particle

Preparation of the nanodisc-20S particle was performed the same as previously described (30). The only difference was that we used more proteins to assemble the nanodisc-20S particle to achieve high concentration. The final sample volume was about 50 μl at a concentration of approximately 5 mg/ml. For the N-terminally truncated SNARE complex, the N-terminal sequence before the two amino acids leading up to layer -7 of each SNARE protein was deleted. The amino acid sequences of the NSF and SNARE proteins used in this study were listed in table S3.

Cryo-EM sample preparation and data collection

Quantifoil Cu R1.2/1.3 grids (Quantifoil Micro Tools GmbH, Germany) were washed in chloroform and air-dried. Aliquots of 4-μl samples at a concentration of approximately 5 mg/ml were loaded onto the grids, which were glow-discharged as routine. Grids were blotted for 2.5 s and plunge-frozen in liquid ethane cooled by liquid nitrogen using a FEI Vitrobot IV (FEI Company). Grids were checked in FEI Tecnai T12 operated at 120 kV to ensure that the thickness of ice was proper for data collection and that there was no obvious preferred orientation observed. Grids were transferred to Titan Krios operated at 300 kV for data collection. Images were recorded on a Gatan K2 Summit direct electron detector operated in super-resolution counting mode following the established dose fractionation data acquisition protocol (38). Images were recorded at a nominal magnification of ×22,500, corresponding to a calibrated super-resolution pixel size of 0.66 Å on the specimen. The dose rate on the detector was set to be ~8.2 counts per physical pixel per second. The total exposure time was 8 s, leading to a total accumulated dose of 50 electrons/Å² on the specimen. Each image was fractionated into 32 frames, each with an accumulation time of 0.25 s. Dose-fractionated images were recorded using a semiautomated acquisition program UCSF Image4 (written by X. Li). Defocus values ranged from -0.8 to $-2.5 \mu m$.

Image processing

Micrographs were binned twofold (yielding a pixel size of 1.30654 Å per pixel) and further motion-corrected with MotionCor2 (39). Defocus values were determined for each micrograph using CTFFIND3 (40). All 2D and 3D classification and refinement were performed using RELION v1.3 (41) or RELION v2.0 (42).

For the autopicking of 20S particles, 3000 20S particles were boxed from 100 micrographs using e2boxer.py in EMAN2 (43). Then, the boxed particles were extracted from micrographs and 2D classified using RELION 1.3. The generated 2D class averages were used as the templates for the subsequent autopicking of 20S particles. A total of 1,371,140 particles were picked up from 5912 micrographs. After 2D and 3D classifications, good classes containing 237,356 20S particles were then subjected to 3D autorefinement, resulting in a 3D reconstruction map of whole 20S particle with a resolution of 4.6 Å.

To further refine the map of the α -SNAP–SNARE subcomplex and the NSF part, which are flexible to each other, the particle segmentation procedure described in our previous work (30, 34) was applied to the 3D reconstruction of the 20S particles. Briefly, to segment the α-SNAP-SNARE subcomplex from 20S particles, the signals corresponding to the NSF-D1D2 part were first subtracted from the raw images. Then, the α-SNAP-SNARE subcomplex particles were reextracted from the raw particle images and served as a new dataset for 2D classification and 3D reconstruction. The N domain of NSF was too flexible and not subtracted from the raw images. Thus, the segmented particles actually contained both the N domains of NSF and the α-SNAP-SNARE subcomplex. The segmented α-SNAP-SNARE particles were further 2D and 3D classified. Good classes containing 97,910 α-SNAP-SNARE particles were selected and then subjected to 3D autorefinement without applying any symmetry, resulting in a final 3D reconstruction map with a resolution of 3.9 Å based on gold-standard Fourier shell correlation (FSC) 0.143 criteria after applying a soft mask around the α -SNAP-SNARE portion. Similar to the processing of the α -SNAP–SNARE subcomplex described above, the NSF part of 20S particles was also

segmented from raw images by subtracting the signals of the α -SNAP–SNARE subcomplex from raw images. A total of 163,942 NSF particles were selected from 2D and 3D classification and then subjected to 3D autorefinement without imposing any symmetry, resulting in a final 3D reconstruction map with a resolution of 3.7 Å after applying a soft mask around the NSF-D1D2 portion. The local resolution map was estimated using ResMap (44). The workflow of data processing is also summarized in fig. S2.

The procedure of focused classification is summarized in fig. S5A. We first performed the whole 20S reconstruction with all of the 237,356 particles by applying the angles obtained from the refinement of the segmented D1D2 part to the whole particles. Then, the D1D2 signals were subtracted from each particle image. The subsequent 3D classification on the modified particles was carried out by applying a mask around the α-SNAP-SNARE subcomplex and the NSF N domain with all particle orientations fixed at the value determined in the whole 20S particle 3D refinement. Following the first round of 3D classification, one class showing poor density was discarded. The particles from the rest of the classes were combined and then reclassified into 12 3D classes. This classification produced six groups exhibiting distinct patterns of the N domains relative to the asymmetric D1 ring. The corresponding particles before density subtraction from each group were selected and refined, yielding 3D maps ranging from 7.3 to 8.2 Å.

To calculate the distributions of the residue of the SNARE complex relative to the NSF-D1D2 part, we first docked the crystal structure of the SNARE complex [protein data bank (PDB) accession code: 1SFC; (2)] into the unsharpened map of the segmented α-SNAP-SNARE subcomplex according to the registers obtained from the atomic model of the SNARE complex (see below) to identify the target residue at the very N terminus of the SNARE complex. Then, the coordinate of the target residue of the SNARE complex (here, we used atom Cα as representative) in the original micrograph could be determined on the basis of the 3D refinement results of the segmented α -SNAP-SNARE subcomplex. Similarly, the coordinate of any residue of NSF-D1D2 (here, we used atom Cα of K304 of NSF as representative) in the original micrograph could be identified on the basis of the data of the segmented NSF-D1D2 part refinement and its atomic model. Then, the shift from the coordinate of the D1D2 residue in the micrograph to that of the target residue of the SNARE complex can be calculated for each particle. Thus, on the basis of these shifts and the angles obtained from the refinement of the segmented D1D2 and using a Gaussian dot generated by EMAN2 as the image of the target residue, the map representing the distribution of the target residue of the SNARE complex relative to the NSF-D1D2 can be 3D reconstructed with the program relion_reconstruct from the RELION package.

Model building and refinement

To build the model for the α -SNAP–SNARE subcomplex, on the basis of the visibility of the extended density corresponding to the longer C terminus of VAMP and the density map of several layers in the central part of the SNARE complex, the crystal structure of the neuronal synaptic fusion complex [PDB accession code: 1SFC; (2)] was docked into the density map by Chimera (45). The different residues between SNAP25B (the protein we used in this study) and SNAP25A (the protein in 1SFC) were manually mutated using Coot (46). The homology model of the *Bos taurus* α -SNAP was created using Modeller (47) with the crystal structure of the vesicular

transport protein Sec17 [PDB accession code: 1QQE; (27)] as template and was docked into the map. Adjustments of backbones and side chains of the SNARE proteins and α -SNAP were performed manually on the basis of the density map in Coot. Then, real-space model refinement was performed in Phenix (48).

To build the model of the NSF-D1D2 part, the homology model of the D1 domain was created using Modeller with the crystal structure of the D1 domain of p97 [PDB accession code: 1E32; (49)] as template. The homology model was docked into the best copy of the six copies of D1 densities in the map by Chimera and manually adjusted in Coot. Then, the D1 model was docked into the other five copies of the D1 densities and further manually adjusted in Coot. The crystal structure of the D2 domain [PDB accession code: 1D2N; (26)] was docked into each of the six copies of the D2 densities. The linker between the D1 domain and the D2 domain was manually built in Coot. Then, the whole model was refined as the α -SNAP–SNARE subcomplex described above.

The atomic models were cross-validated according to previously described procedures (50). Briefly, atoms in the final model were randomly shifted by up to 0.2 Å, and the new model was then refined against one of two half-maps generated during the final 3D reconstruction. FSC values were calculated between the map generated from the resulting model and the two half-maps, as well as the averaged map of two half-maps. We did not observe remarkable separation between FSC_{work} and FSC_{free}, indicating that our model was not over-refined. The statistics of the geometries of the models were generated using MolProbity (51) and listed in table S1. All the figures were prepared in PyMOL (52) or Chimera (45).

α -SNAP-dependent binding of NSF to the maltose-binding protein (MBP)-SNARE complex assay and the MBP-SNARE complex disassembly assay

The α -SNAP-dependent binding of NSF to the SNARE complex assay and the SNARE complex disassembly assay was performed as described before (30, 53). At least three independent experiments were carried out on at least two different batches of purified proteins.

Mouse primary neuronal culture

Hippocampal neurons were dissected from newborn C57/BL6 wild-type mice and incubated in 0.25% trypsin-EDTA (Life Technologies) for 15 min at 37°C. After washing with Hank's balanced salt solution plus 5 mM Hepes (Life Technologies), 20 mM D-glucose, and 2% fetal bovine serum (Gibco), the neurons were mechanically dissociated in culture medium and plated on poly-D-lysine-coated glass coverslips at a density of 50,000 to 100,000 cells/cm². Cells were grown in Neurobasal-A medium (Life Technologies) supplemented with 2% B-27 (Life Technologies) and 2 mM GlutaMAX (Life Technologies). Cultures were maintained at 37°C in a 5% CO₂-humidified incubator.

Lentiviral plasmids and viral preparation

A bicistronic lentiviral vector system, pLox Syn-DsRed-Syn-GFP (pLox), was used by substituting the DsRed coding sequence with the target wild-type or mutant $\alpha\text{-SNAP}$ cDNA sequence. Lentiviral particles were generated by cotransfecting human embryonic kidney (HEK) 293T cells with virus packaging vectors (vesicular stomatitis virus G glycoprotein and $\Delta 8.9$) and the pLox vectors containing the cDNA of interest using polyethylenimine (PEI)

(Polysciences). Virus particles were collected by ultracentrifugation at 25,000 rpm in P28S rotor (Hitachi) in a final volume of 100 μ l. Virus was added to neurons at 3 to 5 days in vitro (DIV), and neurons were analyzed at 16 to 21 DIV.

Electrophysiology

Whole-cell recordings were performed in voltage-clamp mode using a MultiClamp 700B amplifier (Molecular Devices). For primary culture recording, the recording chamber was continuously perfused with a bath solution [128 mM NaCl, 30 mM glucose, 5 mM KCl, 1 mM MgCl₂, and 25 mM Hepes (pH 7.3)] containing 2 mM CaCl₂ via a Warner (Hamden, CT) VC-6 drug delivery system. Fifty-micromolar D-AP5 (*N*-methyl-D-aspartate receptor antagonist; Tocris) and 20-μM bicuculline (γ-aminobutyric acid type A receptor antagonist; Tocris) were applied to isolate AMPA receptormediated mEPSCs. Patch pipettes were pulled from borosilicate glass and had resistances of 3 to 5 megohms when filled with internal pipette solution [130 mM K-gluconate, 1 mM EGTA, 5 mM Na-phosphocreatine, 2 mM Mg-ATP, 0.3 mM Na-guanosine 5'-triphosphate, and 10 mM Hepes (pH 7.3)]. The series resistance was typically <15 megohms and was partially compensated to 60 to 80%. The membrane potential was held at -70 mV. Data were acquired using pClamp10 software (Molecular Devices), sampled at 10 kHz, and filtered at 2 kHz. Off-line data analysis of mEPSCs was performed using Clampfit software (Molecular Devices).

Quantitative reverse transcription PCR

Total RNA was isolated using TRIzol (Life Technologies) according to the manufacturer's instructions. cDNA was synthesized using SuperScript III Reverse Transcription Kit (Life Technologies), and qRT-PCR was performed on a Roche LightCycler 480 PCR System Bio-Rad CFX96 thermal cycler using SYBR green supermix (Bio-Rad) and gene-specific primers. The primer sequences are listed as follows: mouse GAPDH forward, ATGACTCCACTCACGGCAAA; mouse GAPDH reverse, TAGACTCCACGACATACTCAGC; mouse $\alpha\textsc{-SNAP}$ forward, TGACATGCTCAACGCCAAG; and mouse $\alpha\textsc{-SNAP}$ reverse, ATTCCTTCACCGCCTCTGTG. Quantitative analysis was performed using the $\Delta\Delta C_{\rm t}$ method and the glyceraldehyde-3-phosphate dehydrogenase as the endogenous control.

Immunoblot analysis

Neurons were lysed in radioimmunoprecipitation assay buffer [50 mM tris-Cl (pH 8.0), 150 mM NaCl, 1% Triton X-100, 0.5% sodium deoxycholate, and 0.1% SDS] plus a complete protease inhibitor cocktail (Roche). Lysates were centrifuged, and supernatants were subjected to SDS–polyacrylamide gel electrophoresis. The blots were developed using an enhanced chemiluminescence kit (Pierce). Protein levels were quantified by densitometry using NIH ImageJ 1.48 software. Primary antibodies were as follows: anti– α -SNAP antibody (1:500; ab133673, Abcam) and mouse monoclonal antiactin antibody (1:5000; ab6276, Abcam).

Chemical cross-linking of proteins coupled with mass spectrometry (CXMS) analysis

Twenty-microliter purified 20S complexes (reconstituted by wild-type or truncated SNARE chains) at a concentration of about 1 μ g/ μ l were cross-linked at 25°C with 0.25, 0.5, and 1 mM DSS for 1 hour or with 2, 4, and 6 mM EDC hydrochloride/N-hydroxysuccinimide for 2 hours. Reaction with DSS was quenched by the addition of

20 mM NH₄HCO₃, and reaction with EDC was quenched by the addition of 20 mM hydroxylamine·HCl. The cross-linked proteins were then precipitated overnight with six volumes of cold acetone at -2°C . The protein precipitates were dissolved with 10 μ l of 0.1 M tris (pH 8.5) and 8 M urea. After reduction with 5 mM tris(2-carboxyethyl)phosphine hydrochloride and alkylation with 10 mM indole-3-acetic acid, protein samples were digested at 37°C with Lys-C (1:100) for 2 hours followed by trypsin (1:50) overnight.

The digested peptides were analyzed on Q Exactive HF interfaced with Easy n1000. Briefly, the sample was loaded onto a 75-µm by 6-cm trap column (C18, 10 μm resins) that is connected to a 75-µm by 12-cm analytical column (C18, 1.9 µm resins) and then separated with a 70-min gradient (from 0.1% formic acid (FA), 3% acetonitrile (ACN) to 0.1% FA, 30% ACN followed by a 10-min gradient (from 0.1% FA, 30% ACN to 0.1% FA, 80% ACN) and kept at 80% ACN for 10 min. The MS parameters are as follows: Top 20 most intense ions are selected for higher energy collisional dissociation (HCD); resolution is 140,000 in full scan and 17,500 in HCD scan; automatic gain control (AGC) targets are 3×10^6 for fourier transform mass spectrometry (FTMS) full scan and 1×10^5 for tandem mass spectrum (MS)2; minimal signal threshold for MS2 was 4×10^4 ; precursors having a charge state of +3, +4, +5, and +6 are collected; normalized collision energy is 27 for HCD; peptide match is preferred.

The cross-linked peptides were identified with pLink as previously reported (54). After 5% false discovery rate filtering, cross-link peptide pairs were further filtered by requiring more than two spectra counts, best *E* value less than 0.001, and identification in two biological repeat experiments. The cross-linking data were plotted by an online software tool, CX-Circos (http://cx-circos.net).

SUPPLEMENTARY MATERIALS

Supplementary material for this article is available at http://advances.sciencemag.org/cgi/content/full/5/4/eaau8164/DC1

Fig. S1. Cryo-EM analysis of the whole 20S complex, the α -SNAP–SNARE subcomplex, and the NSF-D1D2 part.

Fig. S2. The flowchart for EM data processing.

Fig. S3. Representative raw gel images.

Fig. S4. Analyses of the expression levels of the wild-type α -SNAP and the mutants in the neurons.

Fig. S5. Sequence alignment of $\alpha\textsc{-SNAP}$ from different species.

Fig. S6. Effects of multiple point mutations of VAMP on the α -SNAP-dependent binding of NSF to the SNARE complex.

Fig. S7. Focused 3D classification of the α -SNAP–SNARE subcomplex together with the NSF N domain.

Fig. S8. The N-terminally deleted SNARE proteins can form the 20S complex.

Table S1. Cryo-EM data collection and refinement statistics.

 $Table \, S2. \, CXMS \, analysis \, of \, the \, 20S \, complex \, formed \, with \, either \, wild-type \, SNARE \, proteins \, or \, the \, N\text{-}terminally \, truncated \, SNARE \, proteins.$

Table S3. The amino acid sequences of the NSF and SNARE proteins used in this study.

REFERENCES AND NOTES

- J. S. Bonifacino, B. S. Glick, The mechanisms of vesicle budding and fusion. Cell 116, 153–166 (2004).
- R. B. Sutton, D. Fasshauer, R. Jahn, A. T. Brunger, Crystal structure of a SNARE complex involved in synaptic exocytosis at 2.4 Å resolution. *Nature* 395, 347–353 (1998).
- T. Weber, B. V. Zemelman, J. A. McNew, B. Westermann, M. Gmachl, F. Parlati, T. H. Söllner, J. E. Rothman, SNAREpins: Minimal machinery for membrane fusion. Cell 92, 759–772 (1998).
- R. Jahn, R. H. Scheller, SNAREs—Engines for membrane fusion. Nat. Rev. Mol. Cell Biol. 7, 631–643 (2006).
- D. Ungar, F. M. Hughson, SNARE protein structure and function. Annu. Rev. Cell Dev. Biol. 19, 493–517 (2003).
- D. W. Wilson, S. W. Whiteheart, M. Wiedmann, M. Brunner, J. E. Rothman, A multisubunit particle implicated in membrane fusion. J. Cell Biol. 117, 531–538 (1992).

- A. Mayer, W. Wickner, A. Haas, Sec18p (NSF)-driven release of Sec17p (α-SNAP) can precede docking and fusion of yeast vacuoles. Cell 85. 83–94 (1996).
- T. Hayashi, S. Yamasaki, S. Nauenburg, T. Binz, H. Niemann, Disassembly of the reconstituted synaptic vesicle membrane fusion complex in vitro. EMBO J. 14, 2317–2325 (1995)
- T. Söllner, M. K. Bennett, S. W. Whiteheart, R. H. Scheller, J. E. Rothman, A protein assembly-disassembly pathway in vitro that may correspond to sequential steps of synaptic vesicle docking, activation, and fusion. Cell 75, 409–418 (1993).
- A. P. May, S. W. Whiteheart, W. I. Weis, Unraveling the mechanism of the vesicle transport ATPase NSF, the *N*-ethylmaleimide–sensitive factor. *J. Biol. Chem.* 276, 21991–21994 (2001).
- R. W. Baker, F. M. Hughson, Chaperoning SNARE assembly and disassembly. *Nat. Rev. Mol. Cell Biol.* 17, 465–479 (2016).
- J. A. Ernst, A. T. Brunger, High resolution structure, stability, and synaptotagmin binding of a truncated neuronal SNARE complex. J. Biol. Chem. 278, 8630–8636 (2003).
- A. Stein, G. Weber, M. C. Wahl, R. Jahn, Helical extension of the neuronal SNARE complex into the membrane. Nature 460, 525–528 (2009)
- J. Diao, R. Liu, Y. Rong, M. Zhao, J. Zhang, Y. Lai, Q. Zhou, L. M. Wilz, J. Li, S. Vivona, R. A. Pfuetzner, A. T. Brunger, Q. Zhong, ATG14 promotes membrane tethering and fusion of autophagosomes to endolysosomes. *Nature* 520, 563–566 (2015).
- D. Zwilling, A. Cypionka, W. H. Pohl, D. Fasshauer, P. J. Walla, M. C. Wahl, R. Jahn, Early endosomal SNAREs form a structurally conserved SNARE complex and fuse liposomes with multiple topologies. *EMBO J.* 26, 9–18 (2006).
- W. Antonin, D. Fasshauer, S. Becker, R. Jahn, T. R. Schneider, Crystal structure of the endosomal SNARE complex reveals common structural principles of all SNAREs. *Nat. Struct. Biol.* 9, 107–111 (2002).
- P. Strop, S. E. Kaiser, M. Vrljic, A. T. Brunger, The structure of the yeast plasma membrane SNARE complex reveals destabilizing water-filled cavities. J. Biol. Chem. 283, 1113–1119 (2008)
- J.-K. Ryu, R. Jahn, T.-Y. Yoon, Review: Progresses in understanding N-ethylmaleimide sensitive factor (NSF) mediated disassembly of SNARE complexes. Biopolymers 105, 518–531 (2016).
- M. Zhao, A. T. Brunger, Recent advances in deciphering the structure and molecular mechanism of the AAA+ ATPase N-ethylmaleimide sensitive factor (NSF). J. Mol. Biol. 428, 1912–1926 (2015)
- S. M. Babor, D. Fass, Crystal structure of the Sec18p N-terminal domain. Proc. Natl. Acad. Sci. U.S.A. 96, 14759–14764 (1999).
- A. P. May, K. M. S. Misura, S. W. Whiteheart, W. I. Weis, Crystal structure of the amino-terminal domain of *N*-ethylmaleimide–sensitive fusion protein. *Nat. Cell Biol.* 1, 175–182 (1999).
- R. C. Yu, R. Jahn, A. T. Brunger, NSF N-terminal domain crystal structure: Models of NSF function. Mol. Cell 4, 97–107 (1999).
- C. Zhao, E. A. Matveeva, Q. Ren, S. W. Whiteheart, Dissecting the N-ethylmaleimide– sensitive factor: Required elements of the N and D1 domains. J. Biol. Chem. 285, 761–772 (2010).
- C. Zhao, E. C. Smith, S. W. Whiteheart, Requirements for the catalytic cycle of the N-ethylmaleimide-sensitive factor (NSF). Biochim. Biophys. Acta 1823, 159–171 (2012).
- R. C. Yu, P. I. Hanson, R. Jahn, A. T. Brünger, Structure of the ATP-dependent oligomerization domain of N-ethylmaleimide sensitive factor complexed with ATP. Nat. Struct. Biol. 5, 803–811 (1998).
- C. U. Lenzen, D. Steinmann, S. W. Whiteheart, W. I. Weis, Crystal structure of the hexamerization domain of N-ethylmaleimide–sensitive fusion protein. Cell 94, 525–536 (1998).
- L. M. Rice, A. T. Brunger, Crystal structure of the vesicular transport protein Sec17: Implications for SNAP function in SNARE complex disassembly. Mol. Cell 4, 85–95 (1999).
- E. Bitto, C. A. Bingman, D. A. Kondrashov, J. G. McCoy, R. M. Bannen, G. E. Wesenberg, G. N. Phillips Jr., Structure and dynamics of γ-SNAP: Insight into flexibility of proteins from the SNAP family. *Proteins* 70, 93–104 (2008).
- M. Zhao, S. Wu, Q. Zhou, S. Vivona, D. J. Cipriano, Y. Cheng, A. T. Brunger, Mechanistic insights into the recycling machine of the SNARE complex. *Nature* 518, 61–67 (2015).
- Q. Zhou, X. Huang, S. Sun, X. Li, H.-W. Wang, S.-F. Sui, Cryo-EM structure of SNAP-SNARE assembly in 20S particle. Cell Res. 25, 551–560 (2015).
- T. M. Hohl, F. Parlati, C. Wimmer, J. E. Rothman, T. H. Söllner, H. Engelhardt, Arrangement of subunits in 20S particles consisting of NSF, SNAPs, and SNARE complexes. *Mol. Cell* 2, 539–548 (1998).
- C. Wimmer, T. M. Hohl, C. A. Hughes, S. A. Müller, T. H. Söllner, A. Engel, J. E. Rothman, Molecular mass, stoichiometry, and assembly of 20S particles. *J. Biol. Chem.* 276, 29091–29097 (2001)
- L.-F. Chang, S. Chen, C.-C. Liu, X. Pan, J. Jiang, X.-C. Bai, X. Xie, H.-W. Wang, S.-F. Sui, Structural characterization of full-length NSF and 20S particles. *Nat. Struct. Mol. Biol.* 19, 268–275 (2012).

- Q. Zhou, N. Zhou, H.-W. Wang, Particle segmentation algorithm for flexible single particle reconstruction. *Biophys Rep.* 3, 43–55 (2017).
- H. Kasai, N. Takahashi, H. Tokumaru, Distinct initial SNARE configurations underlying the diversity of exocytosis. *Physiol. Rev.* 92, 1915–1964 (2012).
- K. I. White, M. Zhao, U. B. Choi, R. A. Pfuetzner, A. T. Brunger, Structural principles of SNARE complex recognition by the AAA+ protein NSF. eLife 7, e38888 (2018).
- U. Winter, X. Chen, D. Fasshauer, A conserved membrane attachment site in alpha-SNAP facilitates N-ethylmaleimide–sensitive factor (NSF)–driven SNARE complex disassembly. J. Biol. Chem. 284, 31817–31826 (2009).
- X. Li, P. Mooney, S. Zheng, C. R. Booth, M. B. Braunfeld, S. Gubbens, D. A. Agard, Y. Cheng, Electron counting and beam-induced motion correction enable near-atomic-resolution single-particle cryo-EM. *Nat. Methods* 10, 584–590 (2013).
- S. Q. Zheng, E. Palovcak, J.-P. Armache, K. A. Verba, Y. Cheng, D. A. Agard, MotionCor2: Anisotropic correction of beam-induced motion for improved cryo–electron microscopy. Nat. Methods 14, 331–332 (2017).
- J. A. Mindell, N. Grigorieff, Accurate determination of local defocus and specimen tilt in electron microscopy. *J. Struct. Biol.* 142, 334–347 (2003).
- S. H. W. Scheres, RELION: Implementation of a Bayesian approach to cryo-EM structure determination. J. Struct. Biol. 180, 519–530 (2012).
- D. Kimanius, B. O. Forsberg, S. H. W. Scheres, E. Lindahl, Accelerated cryo-EM structure determination with parallelisation using GPUs in RELION-2. eLife 5, e18722 (2016).
- G. Tang, L. Peng, P. R. Baldwin, D. S. Mann, W. Jiang, I. Rees, S. J. Ludtke, EMAN2: An extensible image processing suite for electron microscopy. *J. Struct. Biol.* 157, 38–46 (2007).
- 44. A. Kucukelbir, F. J. Sigworth, H. D. Tagare, Quantifying the local resolution of cryo-EM density maps. *Nat. Methods* **11**, 63–65 (2014).
- E. F. Pettersen, T. D. Goddard, C. C. Huang, G. S. Couch, D. M. Greenblatt, E. C. Meng, T. E. Ferrin, UCSF Chimera—A visualization system for exploratory research and analysis. J. Comput. Chem. 25, 1605–1612 (2004).
- P. Emsley, B. Lohkamp, W. G. Scott, K. Cowtan, Features and development of Coot. Acta Crystallogr. D Biol. Crystallogr. 66, 486–501 (2010).
- B. Webb, A. Sali, Comparative protein structure modeling using MODELLER. Curr. Protoc. Bioinformatics 47, 5.6.1–5.6.32 (2014).
- P. D. Adams, P. V. Afonine, G. Bunkóczi, V. B. Chen, I. W. Davis, N. Echols, J. J. Headd, L.-W. Hung, G. J. Kapral, R. W. Grosse-Kunstleve, A. J. McCoy, N. W. Moriarty, R. Oeffner, R. J. Read, D. C. Richardson, J. S. Richardson, T. C. Terwilliger, P. H. Zwart, PHENIX: A comprehensive Python-based system for macromolecular structure solution. *Acta Crystallogr. D Biol. Crystallogr.* 66, 213–221 (2010).
- X. Zhang, A. Shaw, P. A. Bates, R. H. Newman, B. Gowen, E. Orlova, M. A. Gorman, H. Kondo, P. Dokurno, J. Lally, G. Leonard, H. Meyer, M. van Heel, P. S. Freemont, Structure of the AAA ATPase p97. *Mol. Cell* 6, 1473–1484 (2000).
- A. Amunts, A. Brown, X.-c. Bai, J. L. Llácer, T. Hussain, P. Emsley, F. Long, G. Murshudov,
 H. W. Scheres, V. Ramakrishnan, Structure of the yeast mitochondrial large ribosomal subunit. Science 343, 1485–1489 (2014).
- V. B. Chen, W. B. Arendall III, J. J. Headd, D. A. Keedy, R. M. Immormino, G. J. Kapral, L. W. Murray, J. S. Richardson, D. C. Richardson, MolProbity: All-atom structure validation for macromolecular crystallography. *Acta Crystallogr. D Biol. Crystallogr.* 66, 12–21 (2010).
- $52. \ L. Schr\"{o}dinger, The \ PyMOL \ Molecular \ Graphics \ System, Version 1.8. \ (Schr\"{o}dinger, 2015).$
- C.-C. Liu, S. Sun, S.-F. Sui, The role of the N-D1 linker of the N-ethylmaleimide–sensitive factor in the SNARE disassembly. PLOS ONE 8, e64346 (2013).
- B. Yang, Y.-J. Wu, M. Zhu, S.-B. Fan, J. Lin, K. Zhang, S. Li, H. Chi, Y.-X. Li, H.-F. Chen,
 S.-K. Luo, Y.-H. Ding, L.-H. Wang, Z. Hao, L.-Y. Xiu, S. Chen, K. Ye, S.-M. He, M.-Q. Dong,
 Identification of cross-linked peptides from complex samples. *Nat. Methods* 9, 904–906 (2012).

Acknowledgments: We thank the staff at the Tsinghua University Branch of the National Center for Protein Sciences Beijing for providing facility support. We thank the "Explorer 100" cluster system of the Tsinghua National Laboratory for Information Science and Technology for providing computation resources. We thank H.-W. Wang, X. Li, and J. Wang for helpful discussion of this project; Y. N. Liu and S. Y. Lu for work in the electrophysiological experiments; D. S. Liu for guidance in the model building; and S. K. Cheppali for the critical reading of the manuscript. Funding: This work was supported by the National Basic Research Program to S.-F.S. (2016YFA0501101 and 2017YFA0504600) and the National Natural Science Foundation of China to S.-F.S. (31670745) and to S.S. (31670746). Author contributions: S.-F.S. initiated and supervised the project; X.H. purified the 20S complex; X.H. and X.W., prepared the EM samples and collected the EM data; X.W., S.S., and Q.Z. performed the EM analysis; X.H., S.S., and F.F. performed the biochemical characterizations; F.F. and S.S. built the atomic models; S.L., Y.C., and M.-Q.D. designed and performed the CXMS assays; Q.-W.W. and J.Y. designed and performed the electrophysiology assays; X.H., S.S., X.W., F.F., and S.-F.S. wrote the

SCIENCE ADVANCES | RESEARCH ARTICLE

manuscript with input from all authors. **Competing interests:** The authors declare that they have no competing interests. **Data and materials availability:** The atomic coordinates of the α -SNAP–SNARE subcomplex and the NSF-D1D2 part have been deposited in the Protein Data Bank with accession codes 6IP1 and 6IP2. The EM maps have been deposited in the Electron Microscopy Data Bank with accession codes EMD–9729 for the overall map, EMD–9697 for the α -SNAP–SNARE subcomplex, EMD–9698 for the NSF-D1D2 part, and EMD–9723 to EMD–9728 for the six states of the 20S complex. Additional data related to this paper may be requested from the authors.

Submitted 17 July 2018 Accepted 19 February 2019 Published 10 April 2019 10.1126/sciadv.aau8164

Citation: X. Huang, S. Sun, X. Wang, F. Fan, Q. Zhou, S. Lu, Y. Cao, Q.-W. Wang, M.-Q. Dong, J. Yao, S.-F. Sui, Mechanistic insights into the SNARE complex disassembly. *Sci. Adv.* 5, eaau8164 (2019).